Concurrently Thermal Reduction and Boron-Doped Graphene Oxide Using Metal-Organic Chemical Vapor Deposition for Ultraviolet Sensing Application

Beo Deul Ryu *, Kang Bok Ko , Min Han , Tran Viet Cuong , Chel-Jong Choi , Chang-Hee Hong *

Posted Date: 25 October 2023

doi: 10.20944/preprints202310.1637.v1

Keywords: reduced graphene oxide; boron; doping; annealing temperature; photodetector

Article

Concurrently Thermal Reduction and Boron-Doped Graphene Oxide Using Metal-Organic Chemical Vapor Deposition for Ultraviolet Sensing Application

Beo Deul ryu [1,*], Kang Bok Ko [1], Min Han [1], Tran Viet Cuong [3,*], Chel-Jong Choi [1] and Chang-Hee Hong [1,2*]

[1] School of Semiconductor and Chemical Engineering, Semiconductor Physics Research Center, Jeonbuk National University, Jeonju, 54896, Republic of Korea; lbd0906@jbnu.ac.kr (B.D.R.); kbko@jbnu.ac.kr (K.B.K.); satbml@gmail.com (M.H.); cjchoi@jbnu.ac.kr (C.-J.C.); chhong@jbnu.ac.kr (C.-H.H.)

[2] LED Agri-bio Fusion Technology Research Center, Jeonbuk National University, Iksan, 54596, Republic of Korea; chhong@jbnu.ac.kr (C.-H.H.)

[3] VKTECH Research Center, Nguyen Tat Thanh University, 298-300A Nguyen Tat Thanh Street, Ward 13, District 4, Ho Chi Minh City, Vietnam; tvcuong@ntt.edu.vn (T.V.C.)

* Correspondence: lbd0906@jbnu.ac.kr (B.D.R.); tvcuong@ntt.edu.vn (T.V.C.); chhong@jbnu.ac.kr (C.-H.H.)

Abstract: We used a metal-organic chemical vapor deposition technique to synthesize a boron-doped reduced graphene oxide (B-rGO) material with various electrical characteristics, dependent on simultaneous reduction and doping procedures. The effect of the doping level on the B bonding in the reduced graphene oxide (rGO) layer controlled by the annealing temperature was investigated using X-ray photoelectron spectroscopy (XPS). The XPS data indicated that the B-rGO layer had a higher B concentration and a considerable number of O-B bonds as a result of the appreciable annealing temperature, which resulted in a decreased work function and Schottky contact between B-rGO and *n*-type Si. Owing to the higher proportion of B-C and B-C_3 bonding in the B-rGO device than that in the rGO/Si device, the lower Schottky barrier height of the B-rGO/*n*-Si vertical junction photodetector resulted in a higher responsivity. This work suggests a facile method of B doping to alter the electrical properties of graphene materials.

Keywords: reduced graphene oxide; boron; doping; annealing temperature; photodetector

1. Introduction

Graphene oxide (GO) is chemically-modified graphene obtained through the modified Hummer's method [1]. Unlike graphene, the as-prepared GO is known as an insulating material. However, its electrical properties can be tailored by modifying the C/O ratio and aromatic sizes, functionalizing with metal, metal oxide, or polymer, and interstitial/substitutional doping with hetero atoms, such as nitrogen (N), phosphorous (P), and boron (B) [2–5]. The use of a hetero atom dopant can convert GO from an insulator to an *n*- or *p*-type semiconductor by employing the appropriate temperature, plasma treatment, and electric field [6–9].

Our group have successfully achieved N- and Ga-doped reduced graphene oxide (rGO) using a metal-organic chemical vapor deposition (MOCVD) system with NH_3 gas and a TEGa source as the N and Ga source, respectively [10,11]. The N-doped rGO materials were obtained using different doping levels with varying NH_3 flow rates at identical annealing temperatures in the MOCVD system. The pulse mode of the doping condition was used to control the dopant level of the Ga-doped rGO materials using the MOCVD system. The system efficiently obtained doped rGO materials using diverse factors, such as the type of dopant source, dopant source volume/rate, and annealing temperature. Therefore, among the various heteroatoms of doped graphene materials, B-doped rGO (B-rGO) has rarely been investigated for different annealing temperatures depending on the

 doi:10.20944/preprints202310.1637.v1

simultaneous thermal reduction and doping processes at identical dopant sources by the MOCVD system.

Uniquely, Lv et al. reported the boron-doped graphene (BG) synthesized by the bubbler-assisted CVD system and BG sheets demonstrated an enhanced sensitivity when detecting toxic gases, such as NO_2 and NH_3 [12]. Otherwise, several research groups reported that the boron-doped rGO materials have chemically synthesized method in aqueous solutions, such as boric acid or boron oxide [7,13–15] Yeam et al reported that the high concentration of B atoms in B-rGO at high annealing temperature increased carrier concentrations that resulted in improved specific capacitance [7] Sahoo et al. reported that the one-pot synthesis of SnO_2-dispersed boron-doped rGO as an anode in Li-ion battery showed comparable performance with a reversible capacity, and two-steps synthesis of SnO_2/BG with a higher amount of boron doping exhibited higher stability over the cycle with an excellent reversible capacity [13]. Prior studies on the peculiar properties of B-doped rGO have frequently been conducted in powder or solution form [13–16]. However, these processes are usually troublesome and inappropriate for large-scale processing when using the B-rGO material platform for optoelectronic device production. To address this issue, we provide, for the first time, a technique for manufacturing B-rGO materials at the wafer scale using the MOCVD system with triethylboron (TEB) as the metal-organic boron precursor. This technology offers great potential for studying and applying B-rGO materials in future optoelectronic devices.

In addition, many studies have employed graphene- and rGO-based materials for photodetection. Some used graphene or rGO as active materials [17–22]. Chitara et al. demonstrated the rGO photoresponse in the UV (at 360 nm) and IR (at 1550 nm) regions and the photodetecting responsivity was found to be 0.12 A/W and 4 mA/W with external quantum efficiencies of 40 and 0.3%, respectively [16–18]. Lai et al. reported that two rGO-based photodetector devices annealed at two different temperatures demonstrated a broadband photoresponse from 290 to 1610 nm covering UV to IR [19]. The device showed lower responsivity and longer response time in the near-IR region than that in the UV to Visible regions. Li et al. demonstrated that *n*-Si and rGO films formed a Schottky contact, and the rGO/*n*-Si *p*-*n* vertical heterojunction structure achieved high photoresponsivity and fast response toward UV-near IR light with zero power consumption [20].

We characterized the electrical properties of B-doped rGO (B-rGO) at various annealing temperatures with respect to simultaneous thermal reduction and doping processes using the MOCVD system. The B1s and O1s peaks observed by X-ray photoelectron spectroscopy (XPS) were used to determine the B bonding configuration and doping level in the B-rGO layer. An investigation of the doping-level dependency of B-rGO layers in *n*-type Si/B-rGO Schottky diodes demonstrated a correlation between the device characteristics and the doping level of the B-rGO layer.

2. Materials and Methods

The synthesis of a graphene oxide (GO) solution with a concentration of 0.5 g/L was described in a previous work [11] using the modified Hummer method. The prepared uniform GO layer was coated onto a cleaned 450 μm-thick *n*-type Si substrate using a spray-coating system. The thickness of the GO layer (20 nm) was measured by atomic force microscopy (AFM) [23]. To produce the rGO layer, as-prepared GO layers were annealed in hydrogen ambient for 10 min inside the MOCVD system at 600, 700, and 800 C, respectively. As compared to the GO thickness, rGO layers became thinner (~10 nm) because of the removal of oxygen functional groups [23]. The triethylboron (TEB, $B(C_2H_5)_3$, SAFC Hitech Ltd) precursor was used as a dopant for the B-rGO layer with a source injection volume of 5 sccm. The effect of annealing temperature on the doping level of the B-rGO layer was investigated, as denoted by B-rGO-600, B-rGO-700, and B-rGO-800, respectively. Figure 1a shows the MOCVD doping and annealing process. Chemical bonding was analyzed using XPS (AXIS-Nova, Kratos) with an Al Kα radiation source (1486.8 eV) in an ultrahigh vacuum chamber (0.933 kPa). The work function was measured using ultraviolet photoelectron spectroscopy (UPS, AXIS-Nova) with a He I ultraviolet source ($h\upsilon$ = 21.2 eV).

For the characterization of the n-Si-based photodetector (PD) device, a 300 nm thick-SiO_2 on the *n*-Si substrate was patterned into a rectangular shape with a size of 600 μm × 450 μm using a

 doi:10.20944/preprints202310.1637.v1

photolithography process and was further treated with buffered oxide etch (BOE) solution for bonding the metal area. Then, the patterned SiO_2/*n*-Si substrate was covered on the rGO or B-rGO layers using the spray-coating and doping methods by MOCVD. The active area of the PD devices (approximately 650 μm × 600 μm) was defined using a photolithography process and an inductively coupled plasma-reactive ion etching process with oxygen plasma. Subsequently, Cr/Au (20/150 nm) was deposited on the front electrode of rGO on a patterned SiO_2 layer using electron beam deposition. The device structure is shown in Fig. 1b. Finally, the In-Ga eutectic paste in contact with a Cu foil was used for the rear electrode. The current-voltage (I-V) characteristics were measured under exposure to a 385 nm UV light-emitting diode (LED) using a semiconductor analysis system (Keithley 4200-MS tech). The responsivity spectrum was recorded using a Xenon lamp (450 W) and by an Oriel Cornerstone 130 1/8m monochromator as a light source.

3. Results

3.1. Dependence on annealing temperature

Although rGO is depicted in Fig. 1c at various annealing temperatures, the XPS spectra of B-rGO are displayed in Fig. 1d to illustrate the role of the boron dopant during the thermal reduction of rGO in the MOCVD system. The successful doping of boron atoms in the rGO crystalline network was demonstrated by the emergence of the B1s peak in the XPS spectra of the B-rGO sample. In the wide-scan spectra, the peaks at 284, 530, and 180 eV correspond to carbon, oxygen, and boron atoms. To learn more about the chemical configuration of the C, O, and B atoms in the XPS spectra, these peaks were deconvoluted and are displayed in Fig. 2 and 3. Every fitting parameter was adjusted according to the literature. The XPS C1s spectra of rGO consist of five kinds of components that are assigned to C–C (284.6 eV), C–O, or C–OH (285.6 eV), C=O (287.2 eV), O=C–OH (288.9 eV), and O–C=O (291.2 eV), as shown Fig. 2a–c [23]. The C/O ratio of rGO samples was ~1.58 (rGO-600), 2.25 (rGO-700), and 2.98 (rGO-800), respectively. Fig. 2d–e display that the O1s peak can be fitted into three peaks at O=C (531.5 eV), O–C (532.6 eV), and C–OH (533.6 eV), respectively [11]. The portion of C=O bonding decreased with increasing annealing temperature. The B-rGO samples exhibited an additional peak at 282.8 eV for C–B bonds due to B-doping, as shown in Fig. 3b and c [24–26]. Agnoli et al. have reported that the boron-doped graphene material form several different functional groups ranging from substitutional boron to boronic (C=B–OH) and borinic (C–B=OH) esters, and organo-borane (C–B–H) according to the Ball model of BG [27]. The C–B bonding portion increased with annealing temperature because of substitutional boron doping, even though the B-rGO-600 sample disappears, as shown in Fig. 3a–c. The annealing temperature increased with the reduction of the oxygen functional groups in rGO; however, the XPS C1s spectra of both B-rGO-700 and B-rGO-800 samples showed an oxygen bonding portion with a high annealing temperature owing to an increase in both boronic and borinic bonds. The XPS O1s spectra showed four-component peaks corresponding to C=O (531.6 eV) and C–O (532.4 eV), C–OH (533.2 eV), and B–O (533.9 eV), respectively, as shown in Fig. 3d–f [26,28]. The presence of the B–O bonding configuration in the B-rGO-600 layer indicated that there were B-doped rGO domains within the B-rGO films. The B-rGO-800 layer has a lower C-OH bonding component, which causes an increase in both boronic and borinic bonds compared to the B-rGO-700 layer. The deconvolution of the XPS B1s spectra at 187.6, 188.3, and 189.1 eV revealed the B–B, B–C, and B–O bondings, shown in Fig. 3g–i [29,30]. The intensity of XPS B1s peak enhances with increased annealing temperature, the B–C bonding of the B-rGO layer means that the substitutional boron dopant is attached to the rGO layer. The XPS spectra showed that the B-rGO layer was formed using the MOCVD method under the aforementioned annealing temperature conditions.

Preprints (www.preprints.org) | NOT PEER-REVIEWED | Posted: 25 October 2023 doi:10.20944/preprints202310.1637.v1

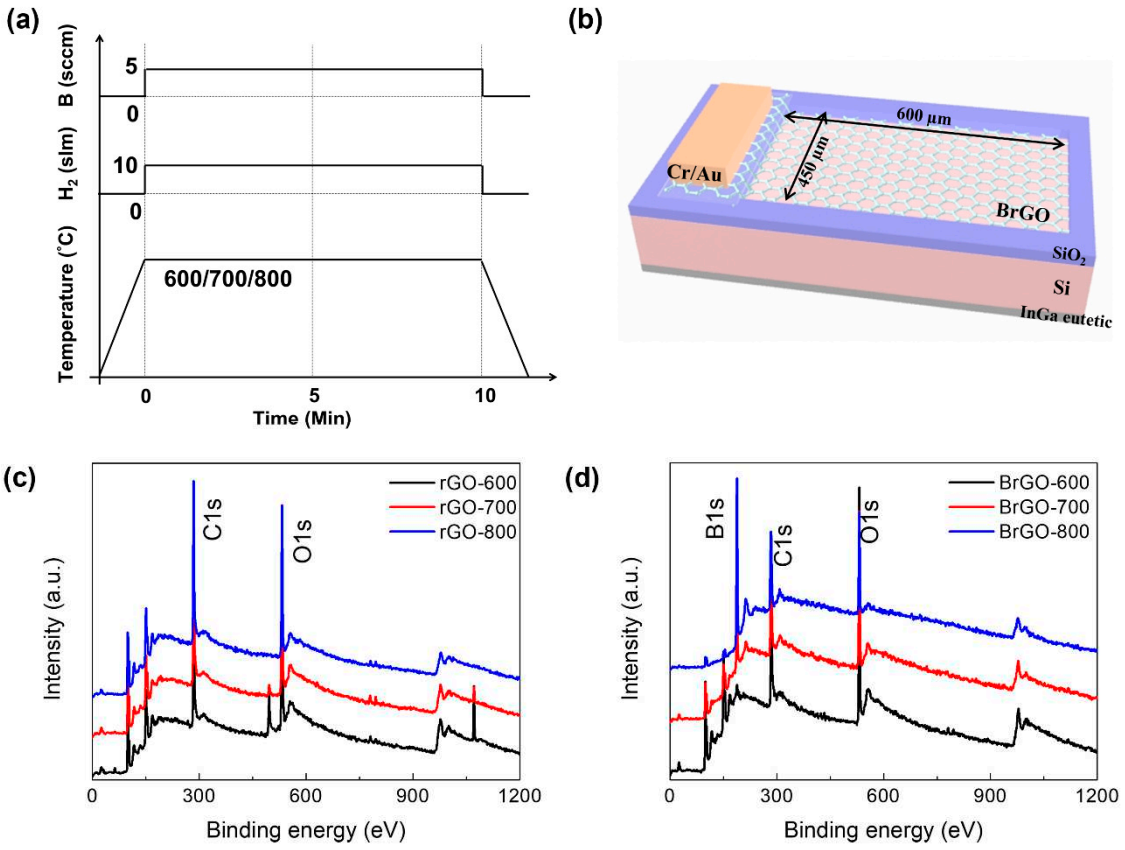

Figure 1. (a) Schematic illustrated image of B-doped rGO with stimulate doping and annealing process, and (b) illustrated image of proposed Si/BrGO vertical structure. XPS spectra of (c) rGO and (d) BrGO with annealing temperature conditions.

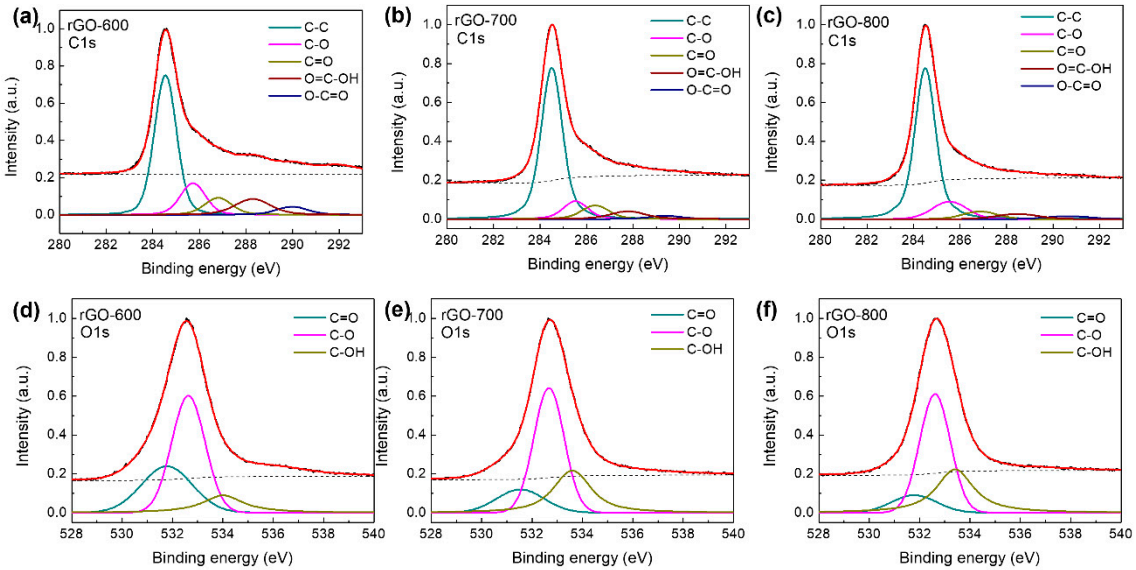

Figure 2. XPS C1s spectra of (a) rGO-600, (b) rGO-700, and (c) rGO-800. XPS O1s spectra of (d) rGO-600, (e) rGO-700, and (f) rGO-800.

Preprints (www.preprints.org) | NOT PEER-REVIEWED | Posted: 25 October 2023 doi:10.20944/preprints202310.1637.v1

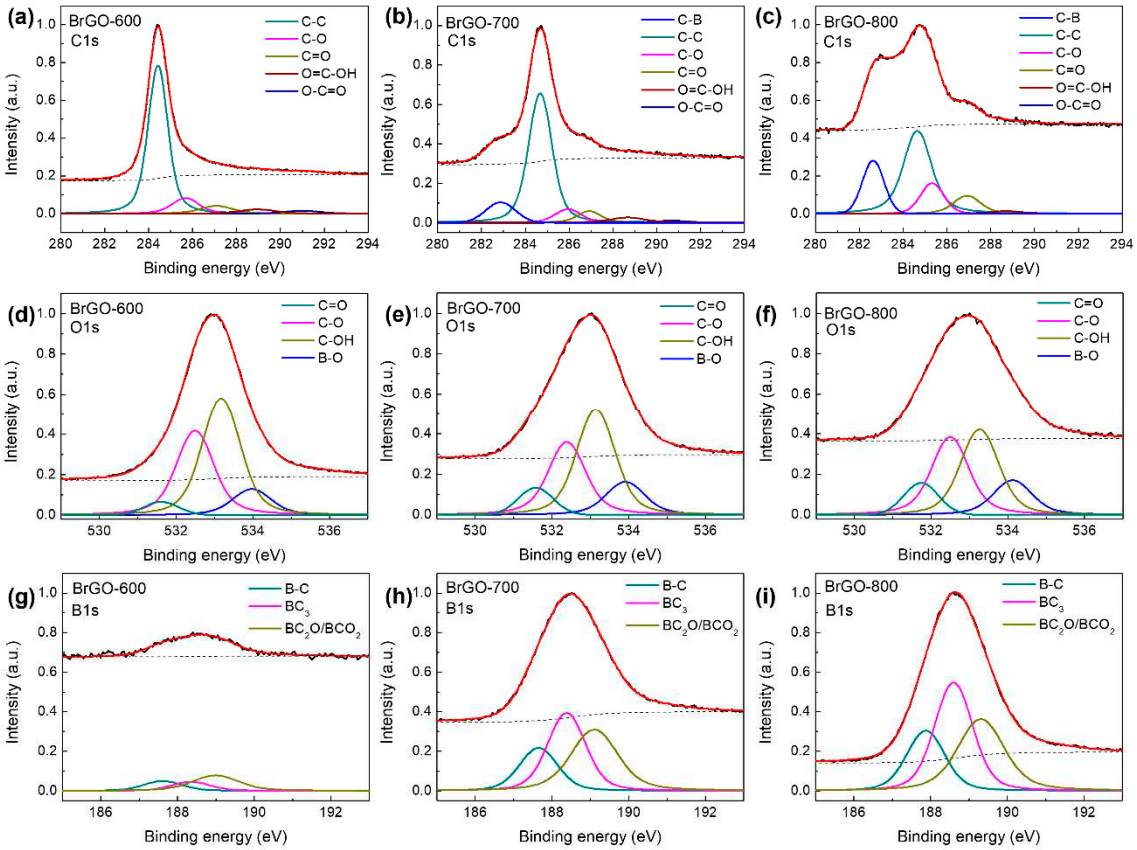

Figure 3. XPS C1s spectra of (a) BrGO-600, (b) BrGO-700, and (c) BrGO-800. XPS O1s spectra of (d) BrGO-600, (e) BrGO-700, and (f) BrGO-800. XPS B1s spectra of (g) BrGO-600, (h) BrGO-700, and (i) BrGO-800.

Tuning the work function of rGO materials is highly anticipated because this electrical parameter is a key factor that affects the optoelectronic device performance. The synthesis and reduction methods used, which typically result in varying aromatic sizes, defect degrees, and the number of functionalized groups on the rGO sheets, cause a significant change in the work function value [11,31]. Therefore, the effect of the boron dopant and the annealing temperature on the tunable work function value must be investigated. Figure 4a and b show the effect of the boron atom as well as the annealing temperature on the B-rGO layer, as determined by UPS measurements. The work function (Φ) was estimated from the empirical relation shown in Eq. 1:

$$\Phi = h\upsilon - (E_F - E_{cutoff}) \quad (1)$$

where hυ, E_F, and E_{cutoff} are the photon energy of the incident light (21.22 eV), the Fermi level edge, and the measured secondary electron cutoff or inelastic low-kinetic-energy cutoff, respectively [31,32]. The E_{cutoff} and E_F values are obtained from UPS spectra. The work function values of the rGO samples were 4.84 (rGO-600), 4.24 (rGO-700), and 4.14 eV (rGO-800). The value of the work function decreases as the annealing temperature rises, since the higher the annealing temperature, the more oxygen functional groups are removed [23]. Aside from that, the work function values of B-rGO samples were 5.12 (B-rGO-600), 4.95 (B-rGO-700), and 4.88 eV (B-rGO-800). Previous studies have reported that the heteroatom-doped rGO sample has a higher work function value than the rGO sample, and the work function value is dependent on the doping concentration [33,34]. These findings suggest that the B atoms were doped into rGO sheets to form a B-rGO layer and that the work function of the B-rGO sample is dependent on the B atom concentration.

Electrical transport measurements of rGO-800 and B-rGO-800 were performed under a vacuum to reveal the doping effect. The rGO (with and without B-doping) FET devices were fabricated with

Preprints (www.preprints.org) | NOT PEER-REVIEWED | Posted: 25 October 2023 doi:10.20944/preprints202310.1637.v1

a back gate on 300 nm-thick SiO_2/Si substrates with 30/100 nm Cr/Au pads, as previously reported in the fabrication of the device [11]. The rGO layer acts as a channel with a length of 20 μm and a width of 350 μm. The I-V characteristics were measured under vacuum conditions at approximately 1 x 10^{-4} kPa. Figure 4c and d show the drain-source current (I_{ds}) versus gate voltage (V_g) and the typical characteristics of rGO back-gate FETs. The voltage (V_{Dirac}) at the Dirac point corresponds to the minimum value of I_{ds}, and the Dirac point of the rGO FETs has a positive voltage for *p*-type behavior. This is attributed to the oxygen functional groups in the rGO channel and the charged impurities from the SiO_2 substrate [11]. The V_{Dirac} is approximately 8 V for the rGO-800 layer and 23 V for B-rGO-800, which implies *p*-type behavior. The shift in the Dirac point indicates that B-doping demonstrates *p*-type doping characteristics. The Fermi level in the energy band gap, which is caused by the presence of the B atom, is located at a lower level than the Dirac level. This means that the dopant caused a dipole moment on the surface of the rGO sheets [35]. From XPS results, it is anticipated that the shifts in the Dirac point by doping were connected to the oxygen atoms attached to the B atoms. We considered both B-rGO-600 and B-rGO-700 layers to verify the *p*-type characteristics, as not shown. Consequently, we believe that GO can be concurrently reduced to form rGO and doped with B using the MOCVD system, making it feasible to manufacture graphene-based optoelectronic devices on a wafer scale.

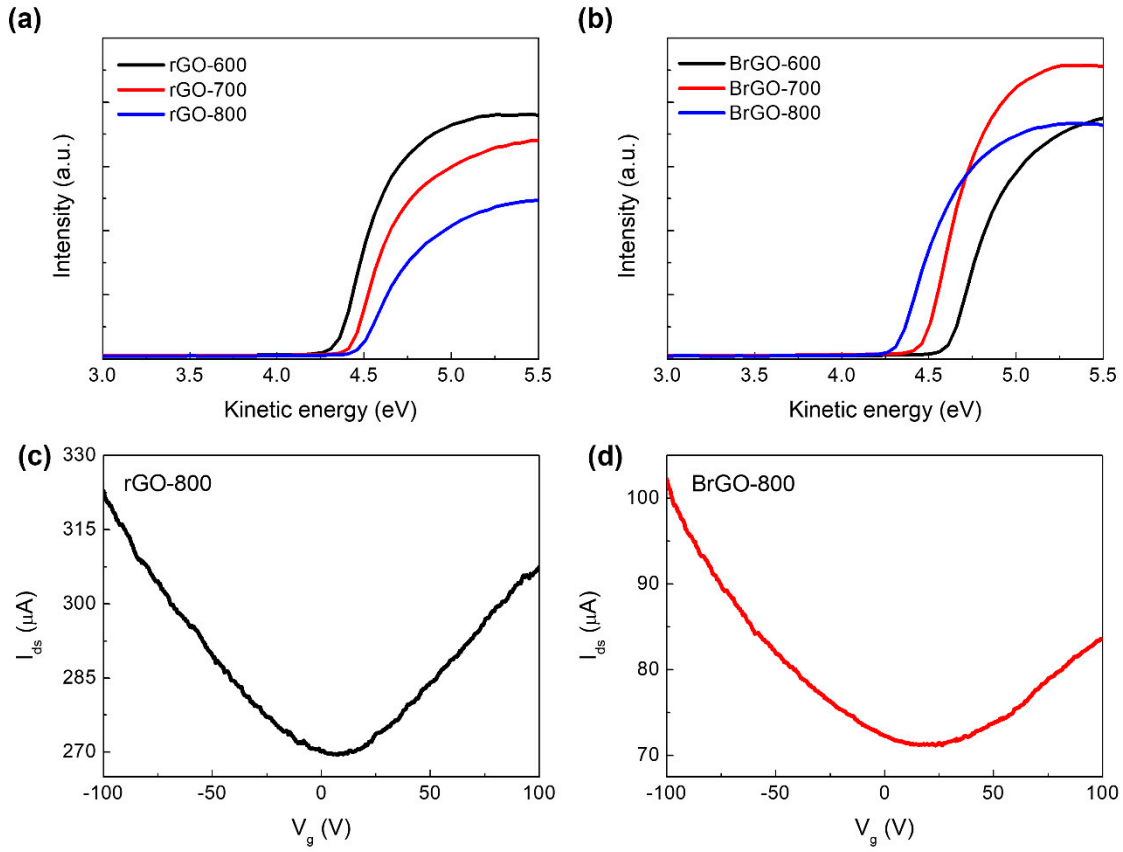

Figure 4. UPS spectra of (a) rGO and (b) BrGO with annealing temperature conditions. Source-drain current versus gate voltage on bottom-gated field-effect transistor structure with (c) rGO-800 and (d) BrGO-800 layers measured with vacuum condition.

Figure 5 shows the UV-Vis absorption spectra of rGO and B-rGO at different annealing temperatures. Generally, GO exhibits a peak at approximately 200 nm, which corresponds to the π-π* transition of the sp^2 C–C bond. The peak of the rGO layer at different annealing temperatures shows a clear red shift of approximately 270 nm. The redshift is attributed to the increase in sp^2 content in the rGO with the annealing process [19]. All rGO layers with different annealing processes have similar peak positions and absorption values. Additionally, the B-rGO samples showed an

Preprints (www.preprints.org) | NOT PEER-REVIEWED | Posted: 25 October 2023 doi:10.20944/preprints202310.1637.v1

absorption peak of approximately 270 nm, which corresponds to the restoration of electronic conjugation on reduction, similar to rGO layers with different annealing temperatures. However, its absorption values are higher than those of the rGO layer [2,36]. B-rGO-800 did not show a peak because of the linear absorption spectra. Yang et al. reported that an increase in the doping level causes a reduction in the redshift because doped free carriers enhance the screening and consequently reduce electron-hole interactions [37]. The linear absorption spectra in B-rGO may be linked to substitutional boron doping levels, which are correlated to the n to π* transitions in the C=B or C–B and C=O bonds. This corresponds to the electron transition from boron states to the π* states, indicating the heterogeneous distribution of boron atoms in the carbon network of the rGO sheets [38]. Eventually, in the UV region (200–400 nm), it seems that the absorption spectra of B-rGO depended on the increased annealing temperature. A steady decrease in light absorption was observed from 400 to 800 nm, which is attributed to the minimization of sp^2 C–C domains in the B-rGO sheets. It implies that the B-rGO with a higher annealing temperature is possible to use the active layer of the PD device in the UV region.

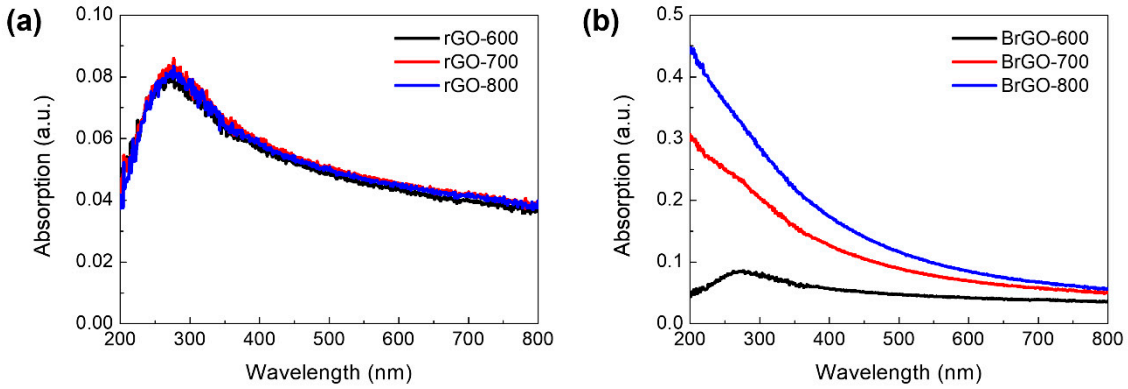

Figure 5. Absorption spectra of (a) rGO and (b) BrGO with annealing temperature conditions.

3.2. Electrical Characterization of B-rGO/n-Si

Figure 6 shows the electrical properties of the rGO and B-rGO layers on *n*-type Si devices annealed at different temperatures under dark conditions. The semi-logarithmic I-V curves of the rGO and B-rGO/Si diodes show Schottky behavior. The diode characteristic of the Schottky junction is described through the thermionic emission theory from dark I-V curves to verify related parameters such as the Schottky barrier height and work function [23], as follows:

$$I=I_s\,[\exp(eV/nkT)-1] \quad (2)$$

and

$$I_s=AA^*\,T^2\exp((-e\Phi_{SBH})/kT) \quad (3)$$

where I_s the saturation current, e is the electronic charge, n is the ideality factor, k is the Boltzmann constant, T is the absolute temperature, A is the active area, Φ_{SBH} is the Schottky barrier height, A* is the Richardson constant of Si (~112 $Acm^{-2}K^{-2}$). Using thermionic emission (TE) theory, the Schottky barrier height of the rGO-600, rGO-700, and rGO-800 were calculated as 0.73, 0.70, and 0.69 eV, respectively [23]. The B-rGO/Si devices also display the Schottky junction, however, the B-rGO/Si device will become the ohmic junction with high annealing temperature (over 900 °C). The calculated Schottky barrier height of Schottky devices was 0.68 eV for B-rGO-600/Si, 0.66 eV for B-rGO-700/Si, and 0.63 eV for B-rGO-800/Si. These results indicate that the built-in electric field in the junction becomes weaker when the Schottky barrier height of the B-rGO-800/Si junction decreases with increasing doping concentration. Thus, we could anticipate the work function, which is the difference in value between the Schottky barrier height of the junction and the electron affinity of *n*-Si concerning the rGO and B-rGO layers. The calculated work function values were approximately 4.78 eV for rGO-600, 4.75 eV for rGO-700, 4.74 eV for rGO-800, 4.73 eV for B-rGO-600, 4.71 eV for B-

Preprints (www.preprints.org) | NOT PEER-REVIEWED | Posted: 25 October 2023 doi:10.20944/preprints202310.1637.v1

rGO-700, and 4.68 eV for B-rGO-800, as calculated using the Schottky-Mott theory. The work function values calculated from the Schottky barrier height appear to be similar to those obtained from the UPS measurements. This confirms that, as the annealing temperature increased, the work function value decreased. The elimination of oxygen functional groups and incorporation of B atoms into the rGO network were facilitated by increasing the temperature. This result demonstrates the advantages of the MOCVD method over the other approaches. We could effectively monitor the removal of oxygen functional groups that occurred simultaneously with the incorporation of B atoms into the rGO network using the MOCVD system. This opens up a new way to modulate the work function of rGO for optoelectronic device applications.

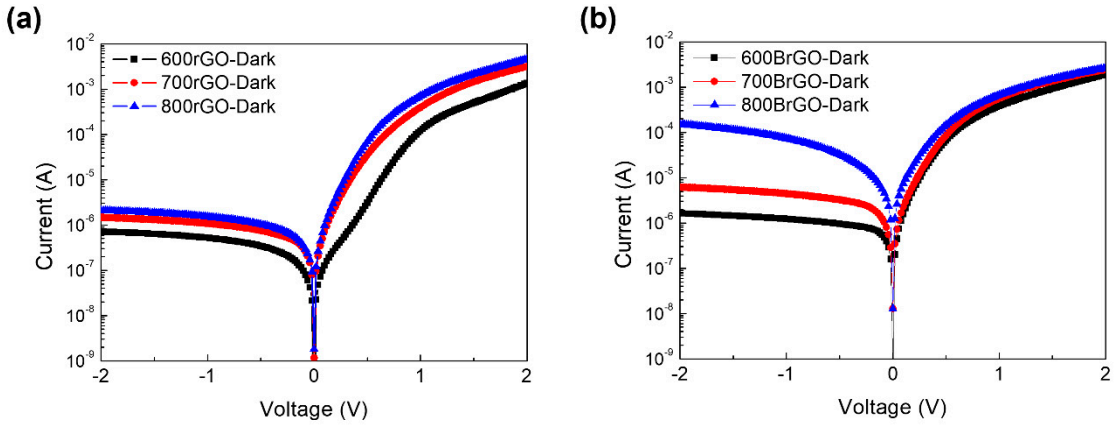

Figure 6. I-V characteristics of (a) Si/rGO and (b) Si/BrGO devices with annealing temperature conditions.

Additionally, photocurrent tests confirmed the photoresponsivity of the doped rGO samples, and the results are summarized in Fig. 7a and b. Light-emitting diodes (LEDs) with a wavelength of 385 nm were used as the illumination source. The rGO/Si heterojunction can be operated as a photovoltaic photodetector at zero bias voltage when illuminated with 385 nm light. Upon light irradiation, the photocurrent decreased with different light intensities from 0.52 to 0.07 mW/cm^2. The photoresponsive phenomenon was reversible, as shown by the immediate dissipation and recovery of the current when the light was turned off and on repeatedly. The photocurrent depends on the light source intensity. All samples exhibited fast photocurrent responses. For rGO, the photocurrent intensity decreased in the order rGO-700 > rGO-600 > rGO-800, which corresponds to Schottky behavior with a Si substrate and a decrease in oxygen functional groups. The deoxygenation of GO was responsible for the decrease in the working mechanism of the rGO layers as the annealing temperature increased. According to previous studies, when numerous oxygen functional groups are withdrawn from GO during the annealing process, the work function value of the rGO layer decreases. In general, the photoexcited carriers can be transformed into an electric current in the rGO/Si device by exploiting the built-in field that accompanies the Schottky barrier to achieve fast separation and transportation of the photogenerated electron-hole pairs. The interface between rGO and Si is well suited to delivering a relatively wide built-in potential (V_{bi} ~ 0.5–0.7 eV) as well as a deletion region [39]. Therefore, it demonstrates that the holes (electrons) can be injected into the rGO layer (Si substrate) when the absorbed photons are efficiently converted into a photocurrent. Consequently, the higher work function of rGO-600 led to a smaller valence band offset between rGO-600 and the Si interface, as compared to rGO-700 [23]. The holes could be better injected into a smaller valence band offset of the rGO-600/Si device under irradiation, while electrons could be suppressed through higher energy height in the energy band. The hole barrier probably prevents the photocurrent at the rGO-700/Si interface, and a smaller electron barrier leads to a higher I_s of rGO-700/Si in dark conditions, as compared to the rGO-600/Si device. Furthermore, the lower photocurrent values of the rGO-800/Si device imply the calculated built-in potential of the rGO-800/Si device is lower than the mentioned value of 0.5–0.7 eV. Consequently, the improved photocurrent of

Preprints (www.preprints.org) | NOT PEER-REVIEWED | Posted: 25 October 2023 doi:10.20944/preprints202310.1637.v1

the rGO-700/Si device results in a lower saturation current (I_s) than those of the rGO-600/Si and rGO-800/Si devices.

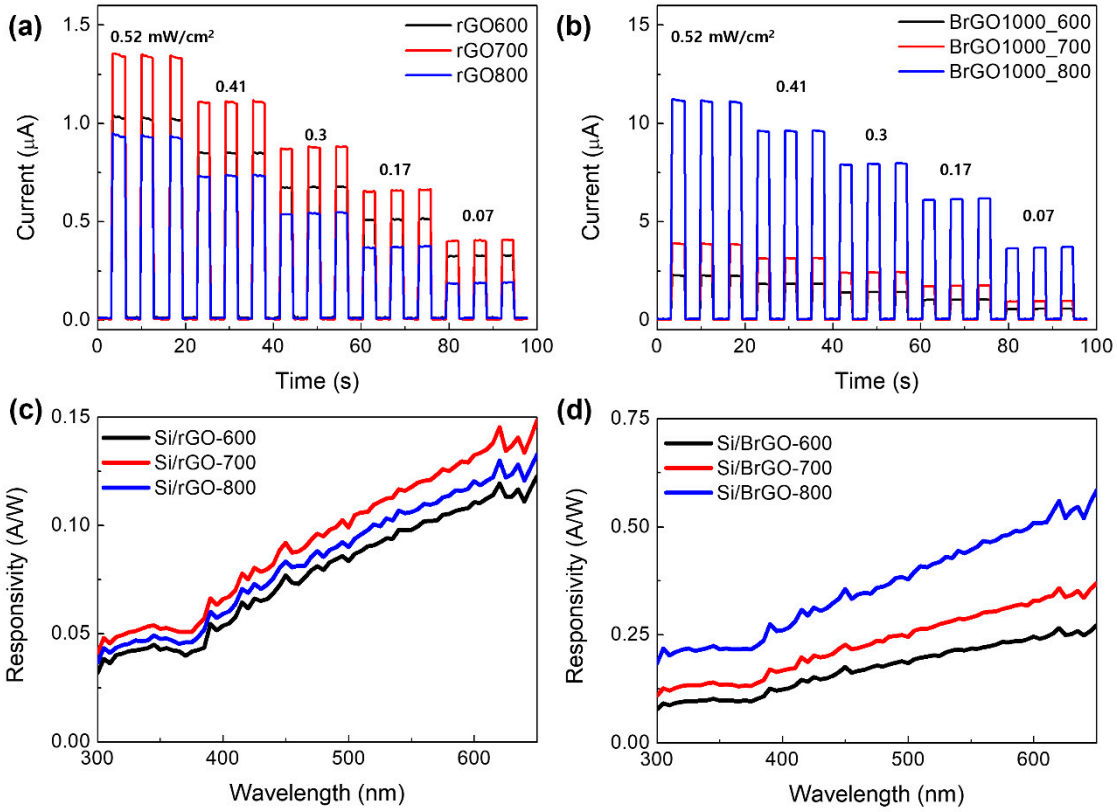

Figure 7. Time-resolved photoresponse of the (a) Si/rGO and (b) Si/BrGO devices under 385nm-UV LED illumination with variable intensity at zero bias voltage. Spectral response of the (c) Si/rGO and (d) Si/BrGO devices were obtained at zero bias voltage.

Otherwise, the photocurrent y-axis values of rGO were 10 times lower than those of B-rGOs. The higher carrier concentration is probably due to the Hall measurement of the B-doped rGO materials. The carrier concentration value is 9.47 x 10^{12} /cm^3 for rGO-600, 3.49 x 10^{13} /cm^3 for rGO-700, 2.40 x 10^{14} /cm^3 for rGO-800, 6.29 x 10^{16} /cm^3 for B-rGO-600, 1.01 x 10^{17} /cm^3 for B-rGO-700, and 3.66 x 10^{17} /cm^3 for B-rGO-800. Further, the sheer resistance of rGO-600, rGO-700, rGO-800, B-rGO-600, B-rGO-700, and B-rGO-800 are 14.2 x 10^3, 10.3 x 10^3, 6.8 x 10^3, 8.2 x 10^3, 6.7 x 10^3, and 4.9 x 10^3 Ω/□, respectively. These findings indicate that the sheet resistance of the rGO layer decreased with an increase in the C/O ratio, and the properties of the B-rGO layer decreased with boron doping. It is to be noted that the photocurrent produced by the B-rGO layer was influenced by both carrier concentration and sheet resistance. The B-rGO photocurrent displayed a decreasing order of B-rGO-800, B-rGO-700, and B-rGO-600, which is coincident with the Schottky behavior of the Si substrate, the lower Schottky barrier height between the BrGO/Si interface, and the increase in B content. The origin of this photoactivity is the addition of various functional groups from the dopants [3]. The B-rGO layer has low sheet resistance and higher carrier concentrations because of the substitutional boronic and borinic bonds in the rGO layer. Therefore, the photoexcited carriers could produce more photocurrent owing to the higher carrier concentration in the B-rGO layer. Furthermore, the interface between B-rGO and Si has a lower Schottky barrier height than the rGO/Si device, allowing photogenerated electron-hole pairs to be easily transferred to the anode/cathode. Accordingly, we assumed that the B-rGO-800/Si device could outperform the rGO-800/Si device in photocurrent efficiency.

Figure 7c and d show the spectral response of the device measured over a spectrum from 300 to 650 mn at zero bias. The responsivity values were reported by considering the proposed area given

by the equation in the TE mode. The photoresponsivities of both the Si/rGO and Si/B-rGO devices increased from 300 to 700 nm. The Si/B-rGO devices have a higher responsivity over the entire spectrum than Si/rGO devices. In particular, at 400 nm, the responsivity of the Si/ B-rGO-800 device was almost five times higher than that of the Si/rGO-800 device. This is evidence of the good performance of Si/B-rGO PD devices in the UV region at 385 nm. Based on the XPS B1s spectra of B-rGO-800, we believe that the boronic and borinic bonding components, that is, the portion of B–C and B–C_3 bonding, are better than the PD performance of Si the B-rGO-800 device. Consequently, the lower work function resulted in a lower Schottky barrier height for Si/B-rGO-800. Theoretically, under UV light illumination, absorption of the incident light results in the generation of electron-hole pairs, which are quickly separated by the built-in electric field and then transferred to the electrodes. The built-in electric field at the junction interface ensures that the device can operate at zero bias voltage. Consequently, Si/B-rGO devices can enhance the photodetector performance with a tunable work function and carrier concentration of B-doped rGO at different annealing temperatures.

4. Conclusions

In this study, we demonstrated that a B-rGO layer was successfully generated by a controlled thermal annealing process using the MOCVD system. Despite the simultaneous thermal reduction and doping operations, the XPS results showed that the concentration of the B atoms connected to the oxygen atoms of the rGO sheets depended on the annealing temperature. Our research demonstrates that B-rGO exhibits controllable electrical and structural features, and doping may be used to modify the work function to improve the performance of optoelectrical applications.

Author Contributions: Conceptualization, B.D.R. and K.B.K.; Methodology, B.D.R., K.B.K. and M.H.; Formal analysis, M.H; Investigation, K.B.K; Resources, C.-J.C.; Data Curation, B.D.R., T.V.C. and C.-J.C.; Writing-original draft, B.D.R. and T.V.C.; Supervision, C.-H.H. All authors have read and agreed to the published version of the manuscript.

Acknowledgments: X-ray photoelectron spectroscopy and ultra-violet photoelectron spectroscopy were analyzed in KBSI. This research was supported by Basic Science Research Program through the National Research Foundation of Korea (NRF) funded by the Ministry of Education (2020R1I1A3A04036537) and by the Technology development Program (S2980806) of Ministry of SMEs and Startups (MSS, Korea).

Conflicts of Interest: The authors declare no conflict of interest.

References

1. Hummers Jr. W. S.; Offeman R. E. Preparation of graphite oxide. *J. Am. Chem. Soc.* **1958**, 80, 1339.
2. Singh M.; Kaushal S.; Singh P.; Sharma J. Boron doped graphene oxide with Enhanced photocatalytic activity for organic pollutants. *J. Photochem. Photobiol.* **2018**, A 364, 130.
3. Putri L.K.; Ng B.-J.; Ong W.-J.; Lee H. W.; Chang W. S.; Chai S.-P. Heteroatom Nitrogen- and Boron-doping as a facile strategy to improve photocatalytic activity of standalone reduced graphene oxide in hydrogen evolution. *ACS Appl. Mater. Interfaces* **2017**, 9, 4558.
4. Tian Y.; Deng C.; Sun Z.; Zhao Y.; Tan T.; Yin F.; Wang X. Facile Hydrothermal synthesis of Sulphur/boron-doped reduced graphene oxide composite cathodes for high-performance Li/S batteries. *Int. J. Electrochem. Sci.* 2018, 13, 3441.
5. Feng L.; Qin. Z.; Huang Y.; Peng K.; Wang F.; Yan Y.; ChenY. Boron-, sulfur-, and phosphorous-doped graphene for environmental applications. *Sci. Total Environ.* **2020**, 698, 134239.
6. Ryu B. D.; Han N.; Han M.; Chandramohan S.; Park Y. J.; Ko K. B.; Park J. B.; Cuong T. V.; Hong C.-H. Stimulated N-doping of reduced graphene oxide on GaN under excimer laser reduction process. *Mater. Lett.* **2014**, 116, 412.
7. Yeom D.-Y.; Jeon W.; Tu N. D. K.; Yeo S. Y.; Lee S.-S.; Sung B. J.; Chang H.; Lim J. A.; Kim H. High-concentration boron doping of graphene nanoplates by simple thermal annealing and their supercapacitive properties. *Sci. Rep.* **2015**, 5, 9817.
8. Li S.; Wang Z.; Jiang H.; Zhang L.; Ren J.; Zheng M.; Dong L.; Sun L. Plasma-induced highly efficient synthesis of boron doped reduced graphene oxide for supercapacitors. *Chem. Commun.* **2016**, 52, 10988.

9. Yu Y.-J.; Zhao Y.; Ryu S.; Brus L. E.; Kim K. S.; Kim P. Tuning the graphene work function by electric field effect. *Nano Lett.* **2009**, 9, 3430.
10. Han M.; Ryu B. D.; Hyung J.-H.; Han N.; Park Y. J.; Ko K. B.; Kang K. K.; Cuong T. V.; Hong C.-H. Enhanced thermal stability of reduced graphene oxide-Silicon Schottky heterojunction solar cells via nitrogen doping. *Mater. Sci. Semicond. Process.* **2017**, 59, 45.
11. Ryu B. D.; Han M.; Ko K. B.; Cuong T. V.; Lim C.-H.; Lee G. H.; Hong C.-H. Gallium dopant-induced tunable electrical properties of reduced graphene oxide using metal-organic organic chemical vapor deposition. *Appl. Sur. Sci.* **2020**, 504, 144500.
12. Lv R.; Chen G.; Li Q.; McCreary A.; B.-Mendez A.; Morozov S. V.; Liang L.; Declerck X.; P.-Lopez N.; Cullen D. A.; Feng S.; Elias A. L.; C.-Silva R.; Fujisawa K.; Endo M.; Kang F.; Charlier J.-C.; Meunier V.; Pan M.; Harutyunyan A. R.; Novoselov K. S.; Terrones M. Ultrasensitive gas detection of large-area boron-doped graphene. *Proc. Natl. Acad. Sci. U. S. A.* **2015**, 112, 14527.
13. Sahoo M.; Ramaprabhu S. One-pot environment-friendly synthesis of boron doped graphene-SnO_2 for anodic performance in Li ion battery. *Carbon* **2018**, 127, 627.
14. Fang H.; Yu C.; Ma T.; Qiu J. Boron-doped graphene as a high-efficiency counter electrode for dye-sensitized solar cells. *Chem. Commun.* **2014**, 50, 3328.
15. Yuan B.; Xing W.; Hu Y.; Mu X.; Wang J.; Tai Q.; Li G.; Liu L.; Liew K. M.; Hu Y. Boron/phosphorous doping for retarding the oxidation of reduced graphene oxide. *Carbon* **2016**, 101, 152.
16. Ngidi N. P. D.; Ollengo M. A.; Nyamori V. O. Tuning the properties of boron-doped reduced graphene oxide by altering the boron content. *New J. Chem.* **2020**, 44, 16864.
17. Chitara B.; Krupanidhi S. B.; Rao C. N. R. Solution processed reduced graphene oxide ultraviolet detector. *Appl. Phys. Lett.* **2011**, 99, 113114.
18. Chitara B.; Panchakarla L. S.; Krupanidhi S. B.; Rao C. N. R. Infrared Photodetectors based on reduced graphene oxide and graphene nanoribbons. *Adv, Mater.* **2011**, 23, 5419.
19. Lai S. K.; Tang L.; Hui Y. Y.; Luk C. M.; Lau S. P. A deep ultraviolet to near-infrared photoresponse from glucose-derived graphene oxide. *J. Mater. Chem. C* **2014**, 2, 6971.
20. Li G.; Liu L.; Wu G.; Chen W.; Qin S.; Wang Y.; Zhang T. Self-powered UV-near infrared photodetector based on reduced graphene oxide/n-Si vertical heterojunction. *Small* **2016**, 12, 5019.
21. Ko K. B.; Ryu B. D.; Han M.; Hong C.-H.; Dinh D. A.; Cuong T. V. Multidimensional graphene and ZnO-based heterostructure for flexible transparent ultraviolet photodetector. *Appl. Sur. Sci.* **2019**, 481, 524.
22. Withers F.; Bointon T. H.; Craciun M. F.; Russo S. All-graphene photodetectors. *ACS Nano* **2013**, 7, 5052.
23. Ryu B. D.; Hung J.-H.; Han M.; Ko K. B.; Park Y. J.; Cuong T. V.; Cho J.; Hong C.-H. Effect of characteristic properties of graphene oxide on reduced graphene oxide/Si schottky diodes performance. *Mater. Sci. Semicond. Process.* **2016**, 44, 1.
24. Yan J.; Tjandra R.; Fang H.; Wang L.-X.; Yu A. Boron acid catalyzed synthesis porous graphene sponge for high-performance electrochemical capacitive storage. *Diamond & Related Materials* **2018**, 89, 114.
25. Balaji S. S.; Karnan M.; Kamarsamam J.; Sathish M. Synthesis of Boron-doped graphene by supercritical fluid processing and its application in symmetric supercapacitors using various electrolytes. *Chem. Electro. Chem.* **2019**, 6, 1492.
26. Hu M.; Yao Z.; Li L.; Tsou Y.-H.; Kuang L.; Xu X.; Zhang W.; Wang X. Boron-doped graphene nanosheet-supported Pt: a highly active and selective catalyst for low temperature H2-SCR. *Nanoscale* **2018**, 10, 10203.
27. Agnnoli S.; Favaro M. Doping graphene with boron: a review of synthesis methods, physicochemical characterization, and emerging applications. *J. Mater. Chem. A* **2016**, 14, 5002.
28. Pandian P. M.; Pandurangan A. Copper annoparticels anchored onto boron-doped graphene nanosheet for use as a high performance asymmetric solid-state supercapacitor. *RSC Adv.* **2019**, 9, 3443.
29. Ranganathan K.; Morais A.; Nongwe I.; Longo C.; Nogueira A. F.; Coville N. J. Study of photoelectrochemical water splitting using composite films based on TiO2 nanoparticles and nitrogen or boron doped hollow carbon spheres as photoanodes. *J. Mol. Catal. A: Chem.* **2016**, 422, 165.
30. Imam M.; Hoglund C.; Jensen J.; Schmidt S.; Ivanov I. G. Trimethylboron as Single-Source Precursor for Boron–Carbon Thin Film Synthesis by Plasma Chemical Vapor Deposition. *J. Phys. Chem. C* **2016**, 120, 21990.
31. Ryu B. D.; Hyung J.-H.; Han M.; Kim G.-S.; Han N.; Ko K. B.; Kang K. K.; Cuong T. V.; Hong C.-H. Long-term stability of Si-organic hybrid solar cells with a thermally tunable graphene oxide platform. *RSC Adv.* **2016**, 6, 72342.

32. Chandramohan S.; Ryu B. D.; Seo T. H.; Kim H.; Suh E.-K.; Hong C.-H. Insights into annealing induced ohmic contact formation at graphene/p-GaN interface with a NiOx contact layer. *J. Phys. D: Appl. Phys.* **2015**, 48, 095102.
33. Hwang J. O.; Park J. S.; Choi D. S.; Kim J. Y.; Lee S. H.; Lee K. E.; Kim Y.-H.; Song M. H.; Yoo S.; Kim S. O. Workfunction-tunable, N-doped reduced graphene transparent electrodes for high-performance polymer light-emitting diodes. *ACS Nano* **2012**, 6, 159.
34. Benayad A.; Shin H.-J.; Park H. K.; Yoon S.-M.; Kim K. K.; Jin M. H.; Jeong H.-K.; Lee J. C.; Choi J-Y.; Lee Y. H. Controlling work function of reduced graphite oxide with Au-ion concentration. *Chem. Phys. Lett.* **2009**, 475, 91.
35. Kang B.; Lim S.; Lee W. H.; Jo S. B.; Cho K. Work-function-tuned reduced graphene oxide via direct surface functionalization as source/drain electrodes in bottom contact organic transistors. Adv. Mater. 2013, 25, 5856.
36. Lai Q.; Zhu S.; Luo X.; Zou M.; Huang S. Ultraviolet-visible spectroscopy of graphene oxide. AIP Adv. 2012, 2, 032146.
37. Yang L. Excitonic Effects on Optical Absorption Spectra of Doped Graphene. *Nano Lett.* **2011**, 14, 3844.
38. Junaid M.; Khir M. H. M.; Witjaksono G.; Tansu N.; Saheed M. S. M.; Kumar P.; Ullah Z.; Yar A.; Usman F. Boron-doped reduced graphene oxide with tunable bandgap and enhanced surface plasmon resonance. *Molecules* **2020**, 25, 3646.
39. Periyanagounder D.; Gnanasekar P.; Varadhan P.; He Jr-H.; Kulandaivel J. High performance, self-powered photodetectors baased on a graphene.silicon schottky junction diode. *J. Mater. Chem. C* **2018**, 6, 9545.